Materials Chemistry and Physics 177 (2016) 206–212

Contents lists available at ScienceDirect

Materials Chemistry and Physics

journal homepage: www.elsevier.com/locate/matchemphys

# Magnetic properties and environment sites in Fe doped $SnO_2$ nanoparticles

S. Ferrari [a, *], L.G. Pampillo [a], F.D. Saccone [b]

[a] Instituto de Tecnología y Ciencias de la Ingeniería "Ing. Hilario Fernández Long", UBA-CONICET, Facultad de Ingeniería, Av. Paseo Colón 850, C1063ACV, Ciudad Autónoma de Buenos Aires, Argentina
[b] Departamento de Física, Facultad de Ingeniería, UBA, Av. Paseo Colón 850, C1063ACV, Ciudad Autónoma de Buenos Aires, Argentina

## HIGHLIGHTS

- The production of nanoparticles of Fe-doped tin dioxide with rutile structure.
- The non-observation of secondary phases (even in Mössbauer Spectroscopy).
- The asymmetry in doublets observed in $^{57}$Fe Mössbauer which means texture effect.
- The magnetic behavior as mainly paramagnetism plus weak ferromagnetism.
- The decrease of ferromagnetism with Fe doping fraction.

## ARTICLE INFO

*Article history:*
Received 24 April 2015
Received in revised form
29 March 2016
Accepted 2 April 2016
Available online 7 April 2016

*Keywords:*
Nanostructures
Semiconductor
Chemical synthesis
Mossbauer spectroscopy
Mossbauer effect
Magnetic properties

## ABSTRACT

$Sn_{1-x}Fe_xO_2$ nanoparticles (x = 0, 0.05, 0.10 and 0.15) were synthesized by co-precipitation. X-ray diffraction and electron diffraction images showed that only rutile type phase was present in the samples. Electron microscopy was used as a tool for revealing morphology, distribution size and structure characteristics of the nanoparticles; while Energy Dispersive X-Ray Spectroscopy analysis confirmed the selected stoichiometry. $^{57}$Fe and $^{119}$Sn Mössbauer spectroscopy at Room Temperature showed a lattice disorder induced by the incorporation of Fe ions in the structure. No magnetic hyperfine ordering was detected for $^{57}$Fe probes and the asymmetry in their quadrupolar splittings is explained as a texture effect at the nanoparticles shells. Quadrupolar splitting at $^{119}$Sn probe reached a maximum for x = 0.1, being this fact attributable to a highest distorted environment. Magnetic hysteresis loops were measured at different temperatures showing, for Fe doped samples, a combination of paramagnetism and weak ferromagnetism.



## 1. Introduction

Tin dioxide is a very promising material because it has high optical transparency, a high band gap (about 3.6 eV) and an electrical conductivity and chemical sensitivity that are very suitable for solar cells, heat mirrors, and catalysis and gas-sensing applications. At the same time, these properties qualify it as a good candidate for its use as Dilute Magnetic Semiconductor (DMS) by doping it with a Transition-Metal (TM) [1,2]. The role of TM doping is not yet fully understood, being a current topic of numerous researches [3–7]. Since room temperature ferromagnetism was theoretically predicted by Dietl et al. [8], various mechanisms have been reported for producing ferromagnetism in DMS. Among them are double-exchange interaction [9] and bound magnetic polarons [10]; also vacancies in the structure has been proposed as origin of this magnetism. Magnetic properties depend strongly on synthesis conditions and dimensionality, the increased surface-to-volume ratio in nanosystems can influence on them. During DMS nanoparticles synthesis, it is a critical point preventing the precipitation of non desired magnetic phases. Even for not very high doping percentages, many authors report secondary phases such as hematite or other iron oxides [11–14]. This highlights the underlying difficulty and the challenge of obtaining a DMS without the presence of secondary phases. Chemical synthesis [15–21] has proven to be a suitable way for achieving such goal.

In this work, we propose studying the effects in the structural

* Corresponding author.
*E-mail address:* sferrari@fi.uba.ar (S. Ferrari).

http://dx.doi.org/10.1016/j.matchemphys.2016.04.020
0254-0584/

and magnetic properties of the incorporation of Fe atoms in $SnO_2$, obtained by chemical co-precipitation synthesis of nanoparticles with $Sn_{1-x}Fe_xO_2$ stoichiometry (x = 0, 0.05, 0.10, 0.15). By X-ray diffraction (XRD) the rutile structure (space group $P4_2/mnm$) of tin dioxide, was confirmed. Scanning Electron Microscopy (SEM) and High Resolution Transmission Electron Microscopy (HRTEM) were used to investigate further the characteristics of the nanoparticles and their structural properties. Fom Mössbauer (MS) with $^{57}Fe$ probe we have found a texture effect (also seen at ref. [22]) that will be discussed in the corresponding section. From MS with $^{119}Sn$ probe we found how the Fe content distorts the structure, reaching a maximum distorsion at x = 0.1. For different temperatures, their hysteresis loops reveals a combined effect of weak ferromagnetism with paramagnetism.

## 2. Experimental

Pure tin dioxide and Fe-doped tin dioxide, according to the formula $Sn_{1-x}Fe_xO_2$ with x = 0.05, 0.10, and 0.15, nanoparticles were prepared by co-precipitation using a slightly modified version of that described in Ref. [17]. In our case the reactants were $SnCl_2.2H_2O$ (Anedra, 99.1% min) and for Fe-doped samples we have used $FeCl_3.6H_2O$ (Tetrahedron, 97% min) (instead of $FeCl_2$ used in Ref. [17]), the final annealing in air was done at 700 °C for 4 h. The obtained powders were characterized by XRD, SEM, Energy Dispersive X-Ray Spectroscopy (EDS), HRTEM, MS with a $^{119}Sn$ probe and $^{57}Fe$ probes; and also by Magnetic Measurements. XRD was carried out with Rigaku D/max diffractometer equipped with a vertical goniometer, using Bragg-Ventano geometry (θ–2θ coupled arms) and Cu-Kα radiation in the $20° \leq 2\theta \leq 95°$ range, measuring at every 0.05° step and sweeping with a 0.4° per minute velocity. SEM and EDS were performed in a Carl Zeiss SMT Supra 40 Scanning Electron Microscope at 3 kV. HRTEM images were obtained using a Philips CM 200 UT microscope equipped with an ultra-twin objective lens; previously to enter the vacuum chamber of the microscope samples were dispersed in isopropyl alcohol and the solution was subjected to ultrasonic agitation during 15 min, after that two or three drops were deposited over ultrathin carbon TEM grids and they were let to dry in air. The Mössbauer measurements were recorded at room temperature (RT) under transmission geometry with a standard constant acceleration spectrometer, using a 10 mCi $Ca^{119}SnO_3$ radioactive source for $^{119}Sn$ MS, and a 5 mCi $^{57}CoRh$ radioactive source for $^{57}Fe$ MS. In both cases data were recorded using a 1024 channel MDAQ107 data acquisition module [23] bcc-Fe was used as standard calibration for $^{57}Fe$ MS and the isomer shift is referred to the corresponding to this phase. Magnetic properties were measured by a Quantum Design PPMS 9T, applying a maximum field of 2T in hysteresis loops at temperatures of 300 (Room Temperature: RT), 200, 150, 100, 50, 35, 15 and 7 K.

## 3. Results and discussion

### 3.1. XRD, SEM, HRTEM and EDS results

X-ray diffraction patterns are shown in Fig. 1 together with Rietveld calculated profile and residuals (at the bottom of each pattern). They exhibit the typical peaks of $SnO_2$ rutile structure (space group $P4_2/mnm$) with no observation of the corresponding to iron oxides or tin monoxide. Then, in the limit of detection for this technique, no other phase segregation occurred during synthesis and Fe was incorporated as a dopant, as it was desired. By a Rietveld analysis of the patterns, we estimated the lattice constant $a$ to lie between 4.746 and 4.753 Å, while lattice constant $c$ lies between 3.189 and 3.195 Å.

The crystallite size extracted from Rietveld analysis has a maximum for the undoped sample with a value of 26 nm, while for doped samples the crystallite size was 11.5 nm for x = 0.05, 9.4 nm for x = 0.10, and 13.8 nm for x = 0.15. In Fig. 2 we show the variation of the unit cell volume, and the ratio of cell constants $c/a$ with the increase of Fe doping fraction. As it can be seen from that mentioned figure the $c/a$ decreases with Fe doping fraction which indicates an expansion in basal plane. Unit cell volume has a maximum at x = 0.1, as also seen in Ref. [18], which can be understood as a greater deformation of the cell.

SEM images can be seen in Fig. 3 showing that the samples are nanoparticles with a spheroidal shape. Particle size distribution was analyzed from these images using ImageTool software. Then, by taking into account the scale, the diameter of particles was measured. The constructed histogram with these data was fitted with a log-normal distribution. The mean values particle sizes obtained from this fitting are displayed in Table 1 and are in good agreement with crystallite size extracted with Rietveld analysis, which states low agglomeration of the samples.

EDS analysis showed that all samples posses just as only elements Sn, O and Fe in case of Fe doped $SnO_2$ powders. The results of atomic percentage composition were extracted with EDS and they are reported in Table 1, where it can be appreciated that the ratio of Fe/(Fe + Sn) resembles quite well the doping fraction stoichiometry as expected for each sample.

HRTEM micrographs, with selected area of electron diffraction (SAED) as inset, are shown in Fig. 4. As it is shown in the images we can confirm the spheroidal shape of nanoparticles. For all cases, in borders can be observed some differences with the nanoparticle cores. Likewise, it can be seen the crystalline planes, and we have obtained their interplanar distances from the radius of electron diffraction rings shown at the SAED. The obtained distances (see Table 2), are fully compatible with tetragonal (rutile) structure of tin dioxide; confirming again the no segregation of undesired phases during the nanoparticle synthesis.

### 3.2. Mössbauer Spectroscopy (MS) results

i) $^{119}Sn$ Mössbauer Spectroscopy

$^{119}Sn$ Mössbauer spectroscopy was performed for all samples. Fig. 5 shows the typical spectra that we obtained in all cases. A doublet corresponding to a quadrupolar hyperfine interaction, originated in an electric field gradient (EFG), can be observed in this figure for samples corresponding to pure tin dioxide (x = 0) and with a small addition of Fe (x = 0.1). Tin probes were found in $Sn^{+4}$ state and no evidence of $Sn^{+2}$ (SnO phase) was detected. The parameters for the lines used to fit the spectra are nearly similar in all cases but as it can be observed, in particular for x = 0.1, the absorption line is broader. Then, we found different values for the hyperfine parameters with a dependence with × as it is shown in Fig. 6. A maximum in both, the quadrupolar splitting (Δ), and isomer shift (δ), is observed for x = 0.1 and the curve profile is similar to the cell volume trend (Fig. 2). The isomer shift δ, for all the doped samples are slightly different from that of pure $SnO_2$, which suggests that a small variation in the Sn–O bond is present for Fe doping. For x = 0.1, δ is positive, which is an indication that depletion in the electron density at nucleus occurs for $^{119}Sn$ probes. The same tendency is observed for Δ and, in this case, the maximum for x = 0.1, gives into account that a higher distortion from the cubic symmetry is present. In fact, for cubic symmetry in the environment of any probe, the EFG nulls and then, Δ = 0. The maximum in the quadrupolar for x = 0.1 is an indication that $^{119}Sn$ probes are located in a higher distorted neighborhood. Then, it can be concluded that these hyperfine parameters strongly depend with the lattice distortion promoted by the Fe doping.

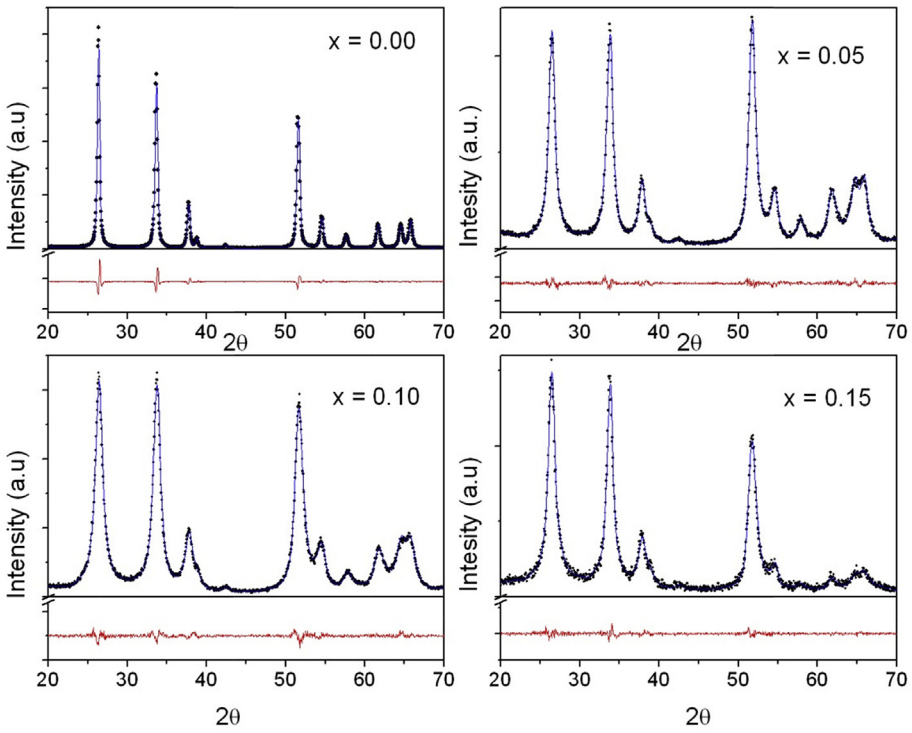


**Fig. 1.** X-ray diffraction experimental (dots) and calculated (blue solid line) all samples. Fe doping fraction indicated as value of x. At bottom of each pattern residuals are displayed. (For interpretation of the references to color in this figure legend, the reader is referred to the web version of this article.)

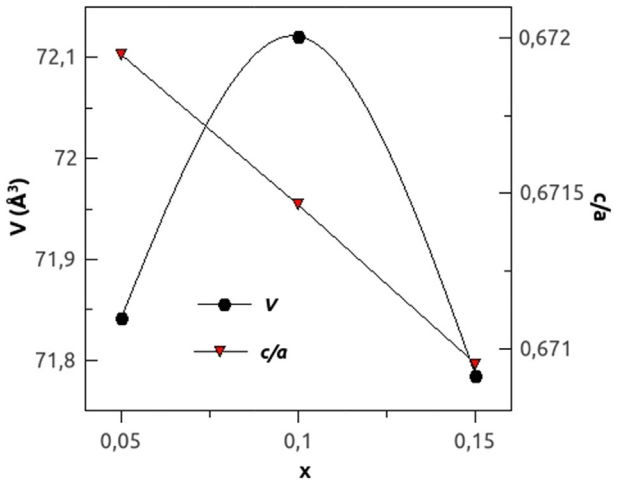


**Fig. 2.** Evolution of unit cell volume and of the ratio of c/a cell constants with the Fe doping fraction.

ii) $^{57}$Fe Mössbauer spectroscopy

$^{57}$Fe Mössbauer spectroscopy, was also performed, in order to give into account how behave their hyperfine fields as a function of doping percentage. No evidence was found of magnetic sextets in all samples' spectra, discarding by this way the presence of iron oxides. In Fig. 7 it is shown two spectra, for an appropriate Doppler velocity range, corresponding to doping concentrations x = 0.1 and 0.15. The insets include the spectra for a Doppler velocity range that would allow to detect magnetic interactions corresponding to Fe-oxides. These last, were taken as different measurements than the corresponding to the low velocity ones. As it can be observed, no evidence of those magnetic interactions is present. We fitted these spectra with two doublets, also corresponding to quadrupolar splittings originated in EFGs. Doublet D1 is assigned to iron ions substituting tin ions, surrounded by six nearest neighbors' oxygen ions, whereas doublet D2 comes from the iron ions also replacing tin ions, surrounded with at least one oxygen vacancy [3,24].

In Table 3 we report the corresponding hyperfine parameters for both $^{57}$Fe sites. There is a good agreement with results reported in previous works (See for example Fig. 2 in Ref. [25]). Due to differences in the population of Fe sites, the D1 doublet has a larger area than the corresponding to D2 and the percentage of this last Fe sites increase for x = 0.15 with respect to x = 0.1. It should be noticed that isomer shift (δ) of this doublet D1 has values consistent with $Fe^{3+}$ (between 0.2 and 0.6 in literature). On the other hand, the absorption spectrum is smaller for x = 0.1 than for x = 0.15, as it is expected, because of its lower Fe content. Also, it can be observed a clear asymmetry in the D1 doublet for x = 0.1, having a ratio between the line 1 to line2 intensities, $R_q = 0.69$. This fact gives into account that the probability of Mössbauer effect is affected by texture, as it is stated from results that were found in similar systems [26] and it is strongly dependent to the alignment of the normal of the absorber plane to the transmission axis as it can be observed from the spectra measured at different velocity ranges. Our result could be associated to that non-spherical particles are realigned with a preferred mean crystallographic orientation for the octahedral with $^{57}$Fe probes in the nanoparticles by pressing during absorber preparation. As it is stated in that reference, our result in the $R_q$ value corresponds to a relative perpendicular orientation between the anisotropy axis and the γ-ray direction. Besides this, the nanoparticles can be thought as divided in two regions as follows, the inner nanoparticle region, named the “core”, and the outer one, the “shell” [22], being this last the most affected by the surface energy. The shell has different physical properties than the core, principally we think that particles at the shell have their anisotropy axes oriented in a direction that is perpendicular to

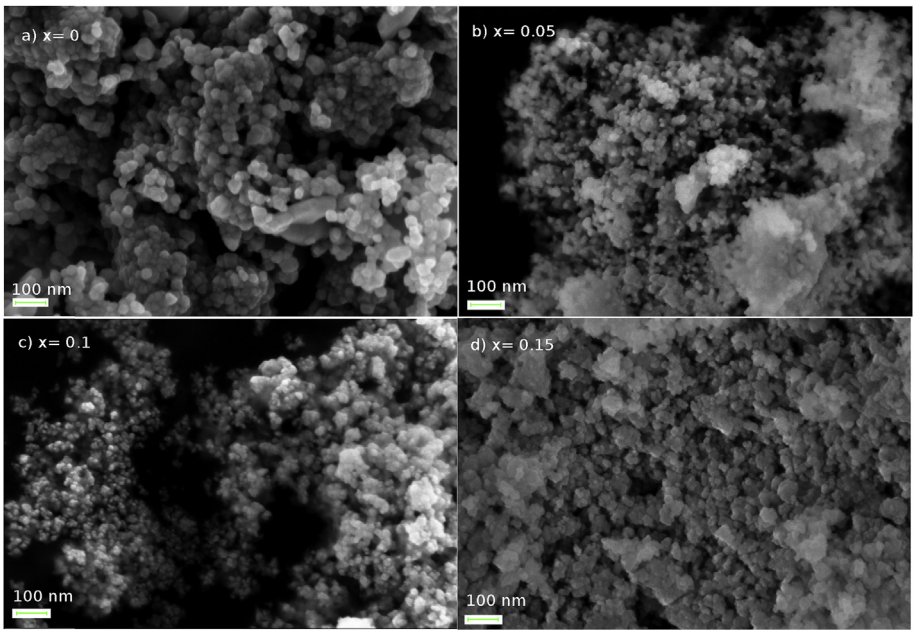


**Fig. 3.** SEM images of samples a) $SnO_2$, b) $Sn_{0.95}Fe_{0.05}O_2$, c) $Sn_{0.9}Fe_{0.1}O_2$, d) $Sn_{0.85}Fe_{0.15}O_2$.

**Table 1**
Atomic percentages obtained from EDS for all samples together with Fe/(Fe + Sn) ratio. Last column reports the mean (and standard deviation as subscript) particle size extracted from the log-normal fitting of histograms constructed analyzing SEM images as described in the text.

| x | ⟨O at.%⟩ | ⟨Sn at.%⟩ | ⟨Fe at.%⟩ | Ratio of at.% Fe/(Fe + Sn) | $\langle d \rangle_{SEM}$ (nm) |
|---|---|---|---|---|---|
| 0.00 | $78_1$ | $22_1$ | 0 | 0 | $30_7$ |
| 0.05 | $77.2_3$ | $21.9_4$ | $0.9_1$ | $0.04_1$ | $18_4$ |
| 0.10 | $76.9_2$ | $21.2_1$ | $1.8_3$ | $0.08_2$ | $18_4$ |
| 0.15 | $81_1$ | $16_1$ | $2.6_2$ | $0.14_2$ | $18_4$ |

**Table 2**
Interplanar distances extracted from the radius of the diffraction rings displayed in the SAED insets of Fig. 4.

| | x = 0 | x = 0.05 | x = 0.1 | x = 0.15 |
|---|---|---|---|---|
| $d_{110}$ (Å) | 3.368 | 3.361 | 3.361 | 3.364 |
| $d_{011}$ (Å) | 2.641 | 2.652 | 2.637 | 2.642 |
| $d_{020}$ (Å) | 2.380 | 2.379 | 2.375 | 2.381 |

the radial one (which coincides with the γ-ray direction for the

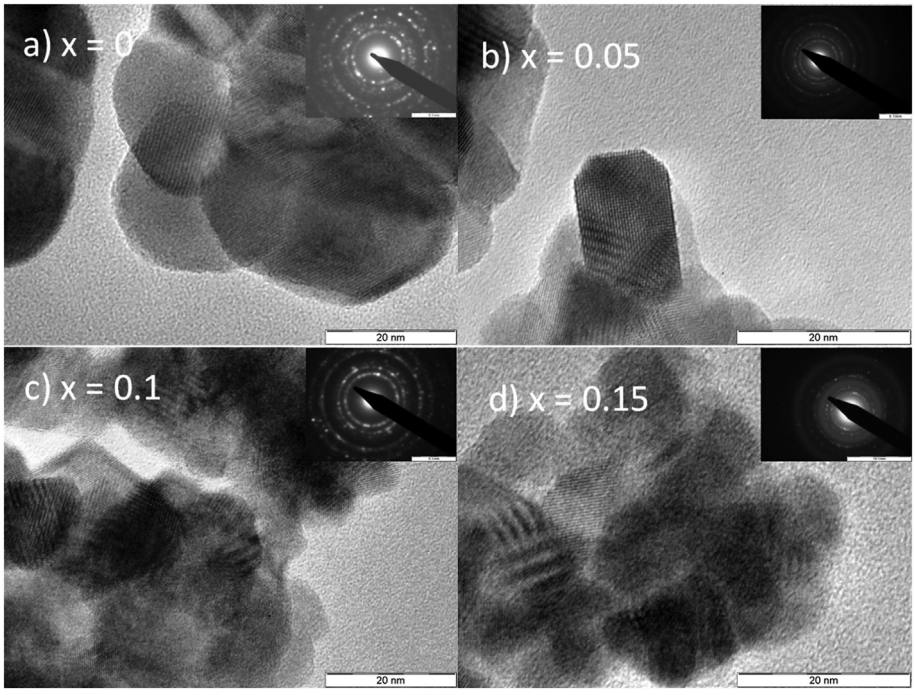


**Fig. 4.** HREM images, with selected area of diffraction as inset at the right upper corner, of samples a) $SnO_2$, b) $Sn_{0.95}Fe_{0.05}O_2$, c) $Sn_{0.9}Fe_{0.1}O_2$, d) $Sn_{0.85}Fe_{0.15}O_2$.

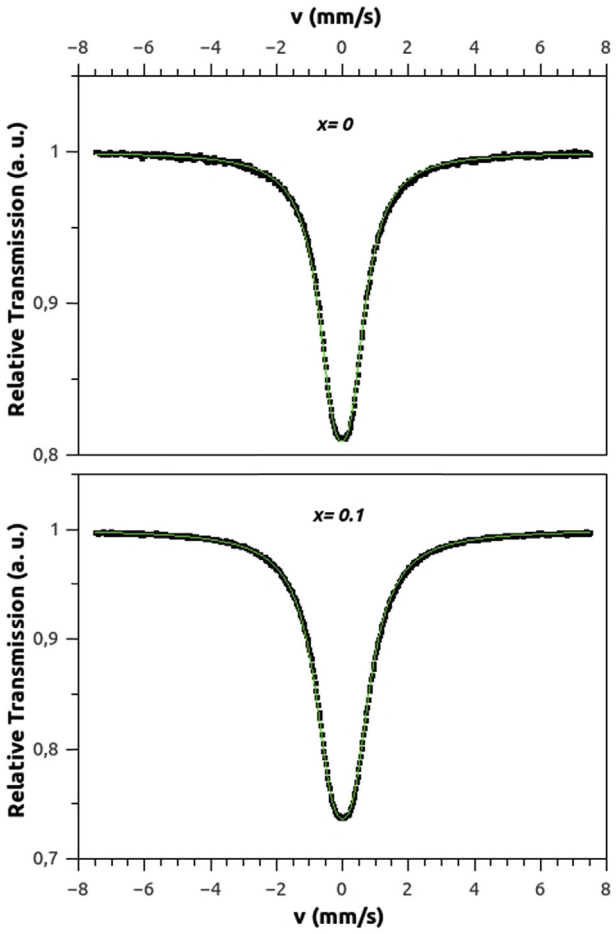


**Fig. 5.** Absorption spectra measured with $^{119}$Sn probe of samples x = 0 (up) and x = 0.1 (down).

effect observed under transmission geometry). It should be also mentioned that, because of this texture effect observed for the D1 site (which has not oxygen vacancies), we assume that we are detecting some $^{57}$Fe probes at surface, being this nanoparticle region with higher content of Fe and Sn atoms oxidized. This doublet asymmetry can also be observed for $^{57}$Fe MS in Ref. [3] in nanoparticles with the same composition, $Sn_{0.9}Fe_{0.1}O_2$ (Table 3).

### 3.3. Magnetic results

In Fig. 8 hysteresis loops taken at room temperature for all samples are shown. All cycles are mainly paramagnetic with a weak ferromagnetic contribution as seen in the inset. We observed Room Temperature Ferromagnetism (RTFM) which cannot be attributed as having its origin from pure iron and/or iron oxides since it was not detected any $^{57}$Fe magnetic phases by MS. So, the magnetic behavior could be attributed to the role of oxygen vacancies, as suggested in Ref. [4]. Table 4 resumes the obtained values by fitting using Eq. (1).

$$M = (2M_s/\pi).\tan^{-1}[(H \pm H_c)/H_c).\tan(\pi(M_r/M_s)/2))] + \chi.H \quad (1)$$

where $M_s$ is the saturation magnetization, $M_r$ is the remanence magnetization, $H_c$ is the coercive field and $\chi$ is the paramagnetic susceptibility. Interestingly as seen from Table 3, the saturation magnetization $M_s$ (which also has the order of memu/g magnitude as in Ref. [4]) decreases with Fe concentration (as in Ref. [3] for

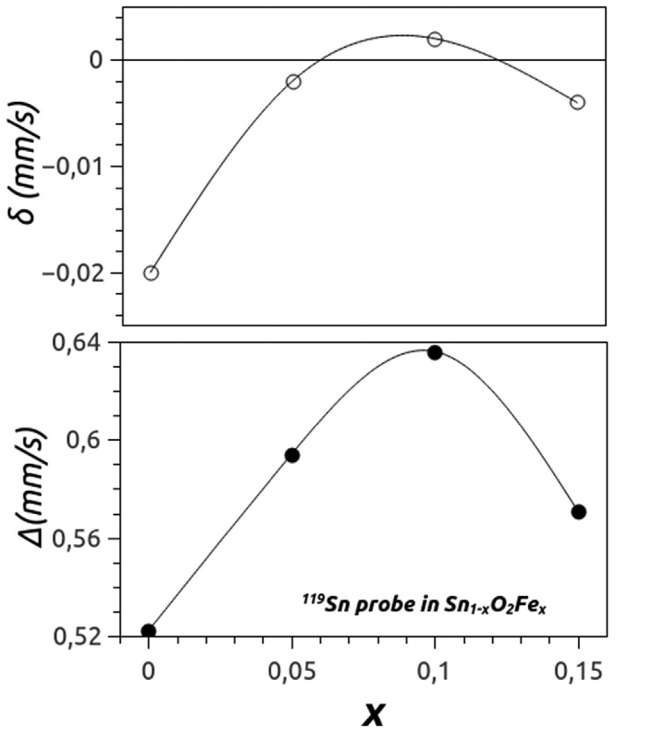


**Fig. 6.** Evolution of hyperfine parameters δ: isomer shift (up) and Δ: quadrupolar splitting (down), extracted from fitting $^{119}$Sn Mössbauer spectra, with Fe doping fraction (x).

concentration higher than 2.5%). This fact reinforces the idea that the magnetism is not only related to the magnetic moment of the dopant. Also this decrease of magnetization in some way discards segregation of iron/iron oxides which would have the contrary effect.

Focusing in the paramagnetic phase of the samples, we have extracted the magnetic susceptibility of each one of the different measured temperatures; the results are displayed in Fig. 9. The inset shows the inverse susceptibility. Inverse susceptibility has been fit to a linear regression according to the Curie-Weiss law [27,28] displayed in Eq. (2):

$$\chi = C/(T-\theta) \rightarrow \chi^{-1} = T.C^{-1} - \theta.C^{-1} \quad (2)$$

where C is the Curie constant and θ is the Weiss constant. Results derived from the linear fit are displayed in Table 5, where it can be seen that mass Curie constant increases linearly with the Fe doping fraction, as expected. From the Weiss constant, that takes account the interaction between elementary magnetic moments, we can see that sample 5% Fe doping fraction has ferromagnetic interactions between elementary magnetic moments, while samples with 10% and 15% doping fraction have antiferromagnetic interactions. This issue could explain also that 5% Fe doping fraction sample has the greatest ferromagnetic saturation magnetization at RT.

From the mass Curie constant we can derive the number of Fe atoms per mol (n), contributing to the paramagnetic state as:

$$n = C.3Ak/(g^2J(J+1)\mu_B^2)$$

(where A is the molecular weight, k is the Boltzmann's constant, g is the Landee's factor (equal to 2, for only spin contribution), $\mu_B$ is the Bohr's magneton and J = 5/2 for spin of iron atoms assuming they

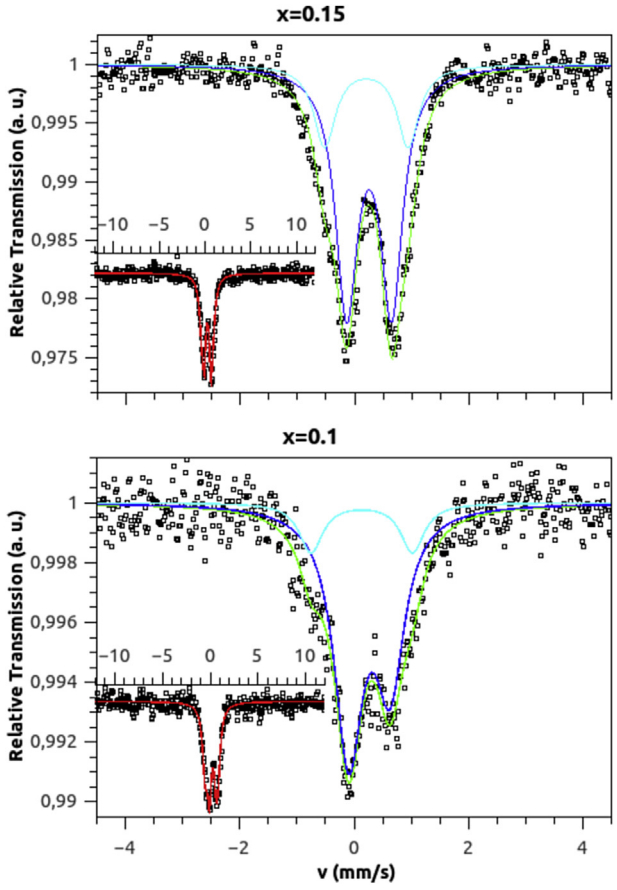


**Fig. 7.** Mössbauer spectra measured with $^{57}$Fe probe for samples x = 0.15 (up) and x = 0.1 (down). The spectra measured for full range Doppler velocity are shown as insets.

are in the $3^+$ oxidation state) and compare it to the total Fe atoms per mol (n' = x.N, where N is the Avogadro's number, and × the Fe doping fraction), to calculate the fraction P = n/n' of n of iron ions in paramagnetic state which is also reported in Table 5. The obtained values of P are similar (but a bit greater) than in Ref. [19] which also uses co-precipitation as chemical method to obtain Fe-doped $SnO_2$ powders and $FeCl_3.6H_2O$ as the precursor for adding the Fe doping atoms.

## 4. Conclusions

Powder nanoparticles of tin dioxide ($SnO_2$) and Fe doped tin dioxide according to the formula $Sn_{1-x}Fe_xO_2$ with x = 0.05, 0.10 and 0.15 synthesized by co-precipitation method have been studied by different experimental techniques. By means of XRD the only crystal phase detected is the rutile from $SnO_2$ discarding, the presence of iron or iron oxides. This fact was also confirmed by $^{57}$Fe MS due to the absence of any magnetic sextet. As a comparison, some authors [11–13] in previous studies have reached a maximum

**Table 4**
Magnetic properties values obtained using Eq. (1) in hysteresis loops.

| | x = 0.05 | x = 0.10 | x = 0.15 |
|---|---|---|---|
| $M_s$ (A/m) | 80.8 | 44.4 | 23.0 |
| $M_r$ (A/m) | 7.6 | 12.5 | 0.8 |
| $H_c$ ($10^3$ A/m) | 8.0 | 20.7 | 3.9 |
| χ (×$10^{-4}$) | 1.12 | 2.47 | 4.49 |

solubility of 10%, obtaining hematite for higher concentrations as a secondary phase, while in this work we extended the solubility up to 15% of Fe without formation of any iron oxide. SEM images of the samples revealed that particles have spheroidal shape, with a diameter between 20 to 30 nm, while crystallite size extracted from Rietveld analysis of the XRD patterns is smaller but with approximately similar values. By EDS analysis we confirmed the stoichiometry expected for each sample. Mössbauer spectroscopy with $^{119}$Sn probe showed an evolution of the hyperfine parameters with the content of iron having a maximum at x = 0.10, which implies that these samples have the highest structural disorder. $^{57}$Fe Mössbauer spectroscopy exhibited two doublets (corresponding to iron atoms substituting tin ones in octahedral sites of rutile structure with or without oxygen vacancies neighbors) with hyperfine parameters similar to those obtained by other authors, with a notorious asymmetry in the subspectra corresponding to the highest fraction of $^{57}$Fe probes. As discussed in the text, this asymmetry can be attributed to the core and shell different distribution of the preferred orientations, being nearly perpendicular between them. This asymmetry was previously observed (see Mössbauer spectra in Refs. [3,17]). However, it has not been clearly explained nor attributed to a texture effect by the authors. Magnetic measurements showed that samples presented a mixture of paramagnetic and weak ferromagnetic behavior, the last standing

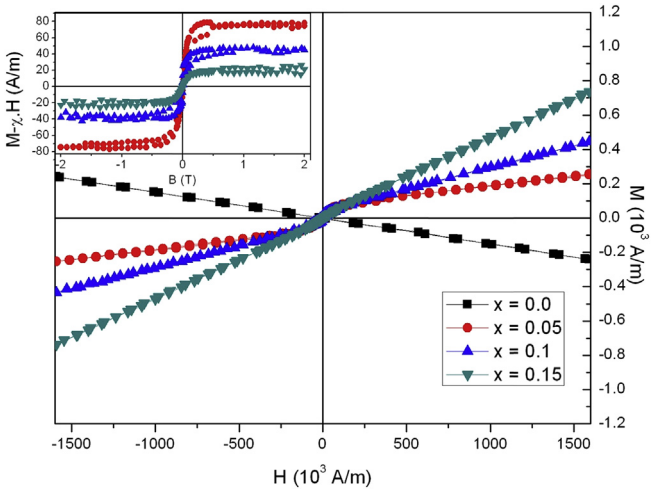


**Fig. 8.** Magnetic Hysteresis cycles of the different samples at Room Temperature (300 K). Inset displays M-χ.H, being χ the paramagnetic susceptibility, evidencing the RT ferromagnetism.

**Table 3**
Values of hyperfine parameters isomer shift (δ), quadrupolar splitting (Δ) together with linewidth (Γ) and area percentage of the doublets found in$^{57}$Fe Mössbauer spectroscopy. Subscripts 1 corresponds to the doublet D1, 2 to the doublet and D2, being explained both in the text. In the reported values we added the errors as a subscript after the last digit.

| x | Δ (mm/s) | $\delta_1$ (mm/s) | $Area_1$ (%) | Linewidth $\Gamma_1$ (mm/s) | $\Delta_2$ (mm/s) | $\delta_2$ (mm/s) | $Area_2$ (%) | Linewidth $\Gamma_2$ (mm/s) |
|---|---|---|---|---|---|---|---|---|
| 0.1 | $0.725_1$ | $0.266_1$ | 83.7 | $0.61_1$ | $1.774_1$ | $0.133_1$ | 16.3 | $0.50_1$ |
| 0.15 | $0.786_1$ | $0.255_1$ | 74.8 | $0.47_1$ | $1.462_1$ | $0.208_1$ | 25.2 | $0.46_1$ |

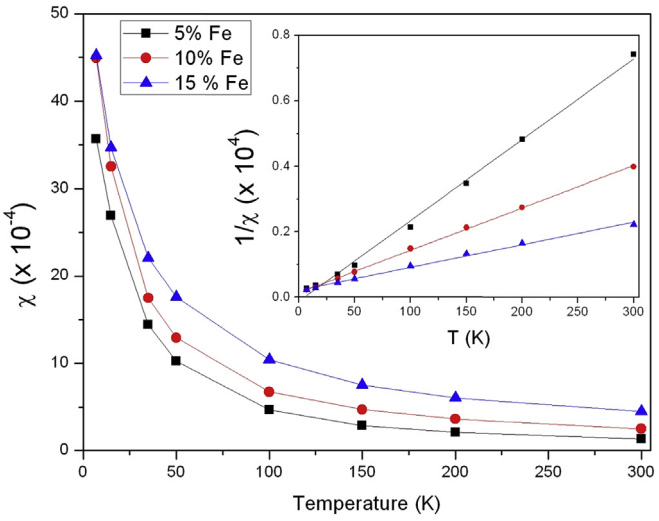


**Fig. 9.** Magnetic susceptibility of the samples versus Temperature (extracted from fit to the magnetic cycles measured at the different temperatures). Inset displays the inverse susceptibility together with their linear fit.

**Table 5**
Mass Curie constant ($C_M$), and Weiss constant (θ) obtained from adjusting the inverse of the paramagnetic susceptibility curves of Fig. 6 to the Curie-Weiss law (AFM stands for Antiferromagnetism and FM for Ferromagnetism), P (%) is the fraction of iron ions in paramagnetic state (calculated).

| | x = 0.05 | x = 0.10 | x = 0.15 |
|---|---|---|---|
| C ($10^{-2}$ K) | 4.03 | 7.67 | 14.4 |
| θ (K) | 4.6 (FM) | −11 (AFM) | −31 (AFM) |
| P | 32 | 29 | 35 |

also at Room Temperature. This ferromagnetism can not be attributed to segregated phases. Paramagnetic susceptibility extracted from cycles at different temperatures shows the typical Curie-Weiss behavior, having a Curie constant linearly with Fe doping fraction. The fraction of Fe ions in paramagnetic state has a minimum for x = 0.1. This fact could be related to the highest disorder for this fraction that was observed at the $^{119}$Sn sites.

In our work we extended the solubility limit of Fe doping in $Sn_{1-x}Fe_xO_2$ (x = 0, 0.05, 0.1 and 0.15) nanoparticles by using a simple co-precipitation method and FeCl3.6H2O instead of FeCl2. By several techniques (XRD, SEM, HRTEM, MS), we confirmed that structural distortions, texture effects and an enhanced shell to core relevance, appeared after synthesis, due to size effects on the nanoparticles (typically, with diameter in the 20–30 nm range). While no Fe magnetic phases were detected by $^{57}$Fe MS, the nanoparticles exhibit a weak ferromagnetic behavior combined with paramagnetism and the magnetic saturation diminishes with doping. Finally, we found that the number of Fe ions at paramagnetic state were found for x = 0.1 in agreement with the highest disorder observed at $^{119}$Sn sites.

## Acknowledgments

The authors thank to ANPCyT (Project PICT 2012 01730) and UBA (Project UBACyT 20020120100113BA) for their financial support. We specially want to thank Corina M. Chanquía and Horacio M. Troiani, from Centro Atómico Bariloche, for their collaboration in adquiring the HRTEM images.

## References

[1] W. Zhou, L. Liu, P. Wu, Nonmagnetic impurities induced magnetism in $SnO_2$, J. Magn. Magn. Mat. 321 (2009) 3356–3359.
[2] J.M.D. Coey, M. Venkatesan, C.B. Fitzgerald, Donor impurity band exchange in dilute ferromagnetic oxides, Nat. Mater. 4 (2005) 173–179.
[3] A. Punnoose, K. Dodge, J.J. Beltrán, K.M. Reddy, Nevil Franco, J. Chess, J. Eixenberger, C.A. Barrero, Dopant spin states and magnetism of $Sn_{1-x}Fe_xO_2$ nanoparticles, J. Appl. Phys. 115 (2014) 17B534.
[4] K. Dodge, J. Chess, J. Eixenberger, G. Alanko, C.B. Hanna, A. Punnoose, Role of oxygen defects on the magnetic properties of ultra-small $Sn_{1-x}Fe_xO_2$ nanoparticles, J. Appl. Phys. 113 (2013) 17B504.
[5] S. Ghosh, M. Mandal, K. Mandal, Effects of Fe doping and Fe-N-codoping on magnetic properties of $SnO_2$ prepared by chemical co-precipitation, J. Magn. Magn. Mat. 3 (2011) 1083–1087.
[6] S.K. Misra, S.I. Andronenko, A. Thurber, A. Punnoose, A. Nalepa, An X- and Q-band $Fe^{3+}$ EPR study of nanoparticles of magnetic semiconductor $Zn_{1-x}Fe_xO$, J. Magn. Magn. Mat. 363 (2014) 82–87.
[7] H. Wang, J. Wei, R. Xiong, J. Shi, Enhanced ferromagnetic properties of Fe+N codoped $TiO_2$ anatase, J. Magn. Magn. Mat. 324 (2012) 2057–2061.
[8] T. Dietl, H. Ohono, F. Matsukura, J. Cibert, G. Ferrand, Zener model description of ferromagnetism in zinc-blende magnetic semiconductors, Science 287 (2000) 1019–1022.
[9] S. Zhou, K. Potzger, Q. Xu, G. Talut, M. Lorenz, W. Skorupa, M. Helm, J. Fassbender, M. Grundmann, H. Schmidt, Ferromagnetic transition metal implanted ZnO: a diluted magnetic semiconductor? Vacuum 83 (2008) S13–S19.
[10] X.X. Wei, C. Song, K.W. Geng, F. Zeng, B. He, F. Pan, Local Fe structure and ferromagnetism in Fe-doped ZnO films, J. Phys. Condens. Matter 18 (2006) 7471–7479.
[11] R. Adhikari, A.K. Das, D. Karmakar, T.V. Chandrasekhar Rao, J. Ghatak, Structure and magnetism of Fe-doped $SnO_2$ nanoparticles, Phys. Rev. B 78 (2008) 024404.
[12] K. Nomura, C.A. Barrero, J. Sakuma, M. Takeda, Room-temperature ferromagnetism of sol-gel-synthesized $Sn_{1-x}$ $^{57}Fe_xO_2$ powders, Phys. Rev. B 75 (2007) 184411.
[13] K. Nomura, A. Shima, Dilute magnetism and Mössbauer study of nanoscaled SnO2 co-doped with Fe, Co, and Sb, prepared by sol-gel method, AIP Conf. Proc. 1489 (2012) 13–20.
[14] J.M.D. Coey, A.P. Douvalis, C.B. Fitzgerald, M. Venkatesan, Ferromagnetism in Fe-doped $SnO_2$ thin films, Appl. Phys. Lett. 84 (2004) 1332–1334.
[15] O. Mounkachi, E. Salmani, H. El Moussaoui, R. Masrour, M. Hamedoun, H. Ez-Zahraouy, E.K. Hlilo, A. Benyoussef, High blocking temperature in $SnO_2$ based super-paramagnetic diluted magnetic semiconductor, J. Alloys Compd. 614 (2014) 401–407.
[16] O. Mounkachi, E. Salmani, H. El Moussaoui, H. Ez-Zahraouy, M. Hamedoun, E.K. Hlilo, A. Benyoussef, Chemical control of superparamagnetic properties of $SnO_2$ diluted magnetic semiconductor, Mat. Lett. 134 (2014) 272–275.
[17] A. Punnoose, J. Hays, A. Thurber, M.H. Engelhard, R.K. Kukkadapu, C. Wang, V. Shutthanandan, S. Thevuthasan, Development of high-temperature ferromagnetism in $SnO_2$ and paramagnetism in SnO by Fe doping, Phys. Rev. B 72 (2005) 054402.
[18] Xavier Mathew, J.P. Enriquez, C. Mejía-García, G. Contreras-Puente, M.A. Cortes-Jacome, J.A. Toledo Antonio, J. Hays, A. Punnoose, Structural modifications of $SnO_2$ due to the incorporation of Fe into the lattice, J. Appl. Phys. 100 (2006) 073907.
[19] V. Bilovol, C. Herme, S. Jacobo, A.F. Cabrera, Study of magnetic behaviour of Fe-doped $SnO_2$ powders prepared by chemical method, Mat. Chem. Phys. 135 (2012) 334–339.
[20] Bin Lu, Changsui Wang, Yuheng Zhang, Electron beam induced crystallization in Fe-doped $SnO_2$ nanoparticles, Appl. Phys. Lett. 70 (1997) 717–719.
[21] S. Music, S. Popovic, M. Metikos-Hucovic, V. Gvozdic, X-ray diffraction and Mössbauer spectra of the system $Fe_2O_3$-$SnO_2$, J. Mater. Sci. Lett. 10 (1991) 197–200.
[22] C. Nayral, E. Viala, P. Fau, F. Senocq, J.-C. Jumas, A. Maisonnat, B. Chaudret, Synthesis of tin and tin oxide nanoparticles of low size dispersity for application in gas sensing, Chem. Eur. J. 6 (2000) 4082–4090.
[23] A. Veiga, M.A. Mayosky, N. Martínez, P. Mendoza Zélis, G.A. Pasquevich, F.H. Sánchez, Smooth driving of Mössbauer electromechanical transducers, Hyperfine Interact. 202 (2011) 107–115.
[24] J. Sakuma, K. Nomura, C. Barrero, M. Takeda, Mössbauer studies and magnetic properties of $SnO_2$ doped with $^{57}$Fe, Thin Solid Films 515 (2007) 8653–8655.
[25] K. Nomura, A. Shima, Dilute magnetism and Mössbauer study of nanoscaled $SnO_2$ co-doped with Fe, Co, and Sb, prepared by sol-gel method, AIP Conf. Proc. 1489 (2012) 13–20.
[26] H.D. Pfannes, U. Gonser, Goldanskii_Karyagin effect versus preferred orientations (Texture), Appl. Phys. 1 (1973) 93–102.
[27] P. Curie, Propriétés magnétiques des corps a diverses températures, Ann. Chim. Phys. 5 (1895) 289–405.
[28] P. Weiss, L'hypothèse du champ moléculaire et la propriété ferromagnétique, J. Phys. Theor. Appl. 6 (1907) 661–690.